Comprehensive characterization of vertical GaN-on-GaN Schottky barrier diodes

P. Vigneshwara Raja, Christophe Raynaud, Camille Sonneville, Atse Julien Eric N'dohi, Hervé Morel, Luong Viet Phung, Thi Huong Ngo, Philippe de Mierry, Eric Frayssinet, Hassan Maher, et al.

Comprehensive Characterization of Vertical GaN-on-GaN Schottky Barrier Diodes

P. Vigneshwara Raja[a,b*], Christophe Raynaud[b], Camille Sonneville[b], Atse Julien Eric N'Dohi[b], Hervé Morel[b], Luong Viet Phung[b], Thi Huong Ngo[c], Philippe De Mierry[c], Eric Frayssinet[c], Hassan Maher[d], Josiane Tasselli[e], Karine Isoird[e], Frédéric Morancho[e], Yvon Cordier[c], and Dominique Planson[b]

[a]Department of Electrical Engineering, Indian Institute of Technology (IIT) Dharwad, Karnataka - 580011, India.
[b]Univ. Lyon, INSA Lyon, Univ. Claude Bernard Lyon 1, Ecole Centrale Lyon, CNRS, Ampère, Villeurbanne Cedex F-69621, France.
[c]Université Côte d'Azur, CNRS, CRHEA, Valbonne 06560, France.
[d]Université de Sherbrooke, CNRS-UMI_LN2, Sherbrooke, Quebec J1K 2R1, Canada
[e]LAAS-CNRS, Université de Toulouse, CNRS, UPS, Toulouse, France.
[*]E-mail: vigneshwararaja@iitdh.ac.in

Abstract:

This paper reports comprehensive characterization of vertical GaN-on-GaN Schottky barrier diodes (SBDs) fabricated on free-standing GaN substrates. The GaN active layer properties are evaluated by atomic force microscopy (AFM), secondary-ion mass spectrometry (SIMS), micro-Raman spectroscopy, cathodoluminescence (CL), and deep-level transient Fourier spectroscopy (DLTFS). The GaN SBDs exhibit near-unity ideality factor (n = 1.1), promising Schottky barrier height (SBH) of Φ_B = 0.82 eV, low turn-on voltage ~0.56 V, leakage current density of $J_R < 5.5\times10^{-6}$ Acm^{-2} at -100 V, breakdown voltage V_{BR} < -200 V, and less interface state density ($N_{SS} < 5\times10^{12}$ eV^{-1} cm^{-2}) at the Ni/GaN Schottky contact. The forward and reverse current transport mechanisms of the SBD are identified by fitting analysis of measured J-V. Weak temperature dependence of Φ_B and n is detected from I-V-T measurements. Similar traps at E_C - 0.18 eV and E_C - 0.56 are identified in the various SBDs from DLTFS, signifying that these traps are omnipresent defects in the epilayer.

Keywords: Free-standing GaN, Schottky barrier diode, current transport, material characterization, defects, DLTFS.

1. Introduction

Due to the rapid advances in the hydride vapour phase epitaxy (HVPE) technique, free-standing GaN substrates are commercially available and open the possibility of developing GaN-based vertical power diodes and transistors like trench MOSFETs [1]. As compared to the high-electron mobility transistors (HEMTs) made-up on heterostructures grown on foreign substrates, the vertical Schottky barrier diodes (SBDs) on homoepitaxial GaN substrate offer several advantages such as latticed matched epilayer, absence of thermal expansion coefficient (TCE) mismatching, reduced dislocation density ($< 10^7$ cm^{-2}) in the active volume, less sensitivity to the surface trapping effects (as the current flows through the vertical direction), and better device scalability [1-4]. The vertical GaN-on-GaN SBDs can deliver high on-state current, low leakage current density, and improved breakdown voltage than the lateral diodes. These performances make the vertical SBDs more suitable for high-power and high-frequency switching electronics. However, the crystal defects (point defects, pits, and dislocations) in the homoepitaxial GaN layers are not fully eliminated, as a result the theoretically projected performance is not yet reached with the GaN SBDs. Hence, the epilayer growth process requires further optimization to mitigate the epilayer defects and to improve the vertical breakdown voltage of the device.

Roccaforte *et al.* [5] analyzed the barrier inhomogeneity and non-ideal electrical characteristics of the vertical SBDs on the free-standing GaN. Various current transport mechanisms controlling the forward and reverse I-V properties of the GaN SBDs were reported [6-10]. Ngo *et al.* [2] identified that the mean dislocation density (total number of dislocations) in the active volume is the deciding factor in affecting the leakage current of the vertical GaN-on-GaN SBDs. In the literature [9-11] several papers reported the SBD characterization results with a relatively good performance. In this paper, we will go one step forward and investigate deeply the SBD properties by gathering the results of different characterization techniques to have a clear view of the GaN bulk quality and the SBD ideality. Indeed, in this work, comprehensive experimental studies (physical, electrical, and trap characterizations) are carried out for the vertical GaN SBDs. The atomic force microscopy (AFM), secondary-ion mass spectrometry (SIMS), micro-Raman spectroscopy [4] and cathodoluminescence (CL) [2] measurements are conducted to inspect the crystalline quality of the Si-doped n-type homoepitaxial GaN layer. The electronic trap levels in the GaN epilayer are investigated by the deep level transient Fourier spectroscopy (DLTFS) technique [12]. Therefore, the obtained results can provide a better understanding of typical characteristics expected for the quasi-ideal vertical GaN-on-GaN SBDs.

2. Experiment

2.1. Epitaxial Growth Process

The 2-inch diameter and 300 µm thick free-standing GaN substrates (with a high n-type doping density of ~2×10^{18} cm^{-3}) supplied by Saint Gobain Lumilog were used for the GaN epilayer growth. The metal-organic chemical vapor deposition (MOCVD) technique was employed for growing the GaN epilayers. In a close coupled showerhead reactor, the carrier gases such as trimethylgallium, ammonia, and hydrogen were introduced to grow the GaN films at a temperature of 1020 °C with 2µm h^{-1} growth rate [2,4]. The doping of the GaN layer was accomplished through the inclusion of diluted silane in a vapor form. Prior to the GaN active layer growth, a thin layer of n^+-GaN buffer (doping in 10^{18} cm^{-3} range) was deposited on the GaN substrate to improve the interface quality between the substrate and the epilayer [4]. Finally, a 5 µm thick lightly-doped, high-quality n^- GaN epitaxial layer was grown on top of the buffer layer. Silicon doping was employed in the GaN active layer with a doping concentration of ~2×10^{16} cm^{-3}. Thus, the homoepitaxial layer structure includes 300 µm thick n^+ GaN substrate, followed by 0.1 µm thin n^+ GaN buffer layer, and 5 µm thick n^- GaN active layer.

2.2. GaN-on-GaN SBD Fabrication

The detailed SBD fabrication process steps are given in our earlier report [2] and are briefly summarized here: As the first step in SBD fabrication, 40 nm thick Ni were deposited on the GaN epilayer using e-beam evaporation. The Ni frames were formed through the standard photolithography and metal lift-off process. Similarly, Ni/Au (40 nm/200 nm) bilayer metal stack was deposited, and the circular Schottky contact patterns were obtained by the photolithography process. On top of that, Au contact pad (200 nm thick) was patterned to enable probing during electrical characterization. The Schottky contacts on the sample surface were insulated by mesa etching of 400 nm depth using reactive ion etching (RIE) based on $Cl_2/Ar/CH_4$ chemistry. The four-layer metal stack Ti/Al/Ni/Au (30nm/180nm/40nm/200nm) was deposited for the back Ohmic contact. The low metal work function of Ti (4.3 eV) can make an Ohmic contact with the highly doped (~2×10^{18} cm^{-3}) n^+ GaN substrate without thermal annealing. Hence, the samples were not undergone for the annealing after the back contact formation.

The schematic cross-section of the fabricated vertical GaN-on-GaN SBD is shown in Fig. 1. The circular Ni/Au based Schottky contacts, and Au contact pads are visualized in the optical microscopic image in Fig. 2(a). The mesa isolation pattern is 10 µm wider than the circular Schottky contact, as seen in the scanning electron microscope (SEM) image in Fig. 2(b). The fully processed GaN sample contains an array of rectangular Ni frames. As depicted in Fig. 2(a), four diodes are located inside each Ni frame, with three different Schottky contact diameters (*d*) such as 200 µm, 100 µm, and two numbers of 50 µm.

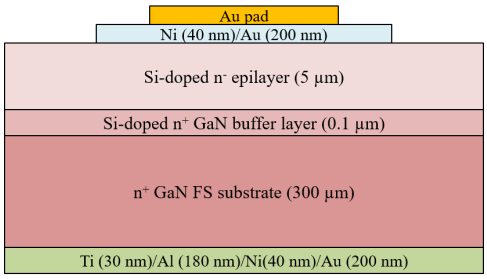

Fig. 1. Schematic cross-section of the vertical Ni/GaN-on-GaN SBD structure.

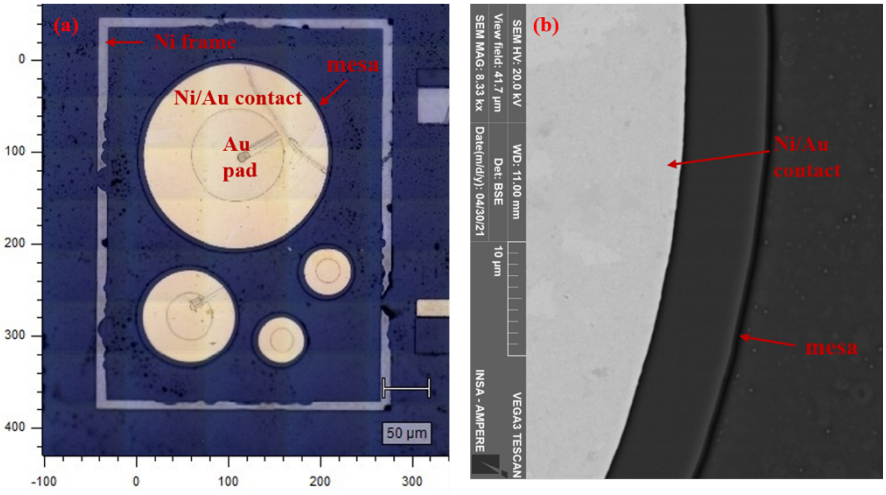

Fig. 2. (a) Optical microscopic of the fabricated SBDs. (b) SEM image of the diode illustrates the mesa isolation depth (mesa pattern 10 µm wider than the Schottky contact).

2.3. Characterization Methodologies

The surface morphology of the GaN epilayer was examined by atomic force microscopy (AFM). The secondary-ion mass spectrometry (SIMS) measurements were carried out to probe the doping concentration profile in the GaN active layer. Prior to the Schottky metal deposition (after Ni frame formation), cathodoluminescence (CL) characterization was carried out within the Ni frame to track the dislocations in the active area of the diodes. The CL imaging of the epilayer was acquired with 10kV accelerating voltage and 500× or 1000× magnification at room temperature (RT). The Renishaw inVia^{TW} confocal Raman microscope [13] was used to investigate the stress in the epilayer with 1 µm spatial and 0.1 µm spectral resolutions. The samples were non-invasively scanned in backscattering geometry at RT by using 532 nm laser light with 100 mW optical power (but only 10% was used to avoid sample heating), 2400 l/mm diffraction grating, and 100× objective lens. The Raman spectrometer calibration was accomplished with a silicon reference Raman shift of 520.5 cm^{-1} prior to each experiment. The studied samples were scanned to perform Raman measurement with a lateral step of 1 µm and a depth step of 1 µm. After curve fitting analysis of Raman phonon spectra, volume mapping of the epilayer was attained in the WiRE 5.4 software interfaced PC. Further details of the µ-Raman measurement procedure are given in our recent report [4].

Keithley 2410 source measure unit (SMU) was utilized to measure the I-V properties of the SBDs at RT. Current-voltage-temperature (I-V-T) experiments were conducted over the temperature range of 293 K to 393 K using the DC probe station to investigate the temperature dependence of the SBH behaviour.

For the DLTFS experiment, the diode-under-test (DUT) was mounted on the sample holder of the Janis cryostat, whose temperature was controlled and varied by the Lakeshore 336 temperature controller and the compressor cooling system. The electrically active traps in the SBDs were filled by using a reduced reverse bias pulse from V_R = -10 V to V_P = -0.1 V for 100 μs width. Following the voltage pulse, the quiescent reverse bias V_R = -10 V was retained and the resultant capacitance transients were measured for an emission transient period of 204.8 ms by using Boonton 3200 capacitance meter. The transient signals were further processed by the digital data acquisition (DAQ) system and finally the transients were recorded in the PhysTech FT1030 software package. Before performing the actual DLTFS measurements, the sample stage (DUT) was cooled down to a low temperature of ~50 K. After that the sample temperature was increased with a fixed heating rate up to 400 K. During the thermal ramp-up, capacitance transients were acquired at a frequent temperature interval. Based on the work of Weiss *et al.* [12], the discrete Fourier coefficients were computed for each capacitance transient. The Fourier coefficients carry the information of emission time constant and transient amplitude associated with the trap level [12,14], thus it is possible to directly extract the trap parameters through a single temperature scan (50 K to 400 K).

3. Results and discussion

3.1. GaN Epilayer Features

Figures 3 shows the AFM image acquired on the surface of the GaN epilayer with a scanning area of 2×2 μm^2. The well-aligned atomic patterns are noticed along with the absence of pits and hillocks [2,9,15], thereby yielding a smoother surface with the root mean square (RMS) roughness of 0.16 nm in the studied sample. Figure 4 illustrates the Si doping concentration distribution profile in the GaN active layer identified from the SIMS measurements. Close to the surface, very high Si concentration is noticed from the SIMS profile in Fig. 5, as similar to the literature reports [16-18]. The depth of this dopant tail from the surface to the bulk is about 100 nm. The tail formation may be visualized as follows [16]: During SIMS measurements, the primary ion-beam sputtering can knock the dopant atoms from surface contaminations into a certain depth (about 50 nm) in the epilayer. The tails can be further extended due to the out-diffusion process through the dislocations and grain boundaries. However, beyond this tail (~100 nm), a nearly uniform Si doping density (~2.5×10^{16} cm^{-3}) is observed in the epilayer. A thin layer of highly-doped GaN is regrown on top of the free-standing GaN substrate to ensure that the series resistance will not be limited by the interface contamination (particularly with carbon impurity). For this reason, high concentration of Si-dopants is detected in the

regrown region located beyond the depth of 4.2 µm. Overall, the SIMS results reveal that the silicon doping concentration is almost uniform (~2.5×10^{16} cm^{-3}) in the GaN active layer.

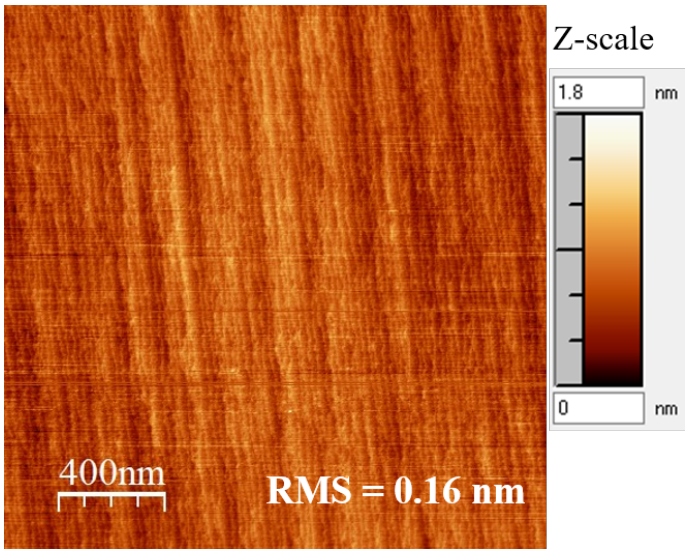

Fig. 3. AFM image acquired on GaN epilayer surface with a scanning area of 2×2 μm^2. A smooth surface with RMS roughness of 0.16 nm obtained in the studied sample.

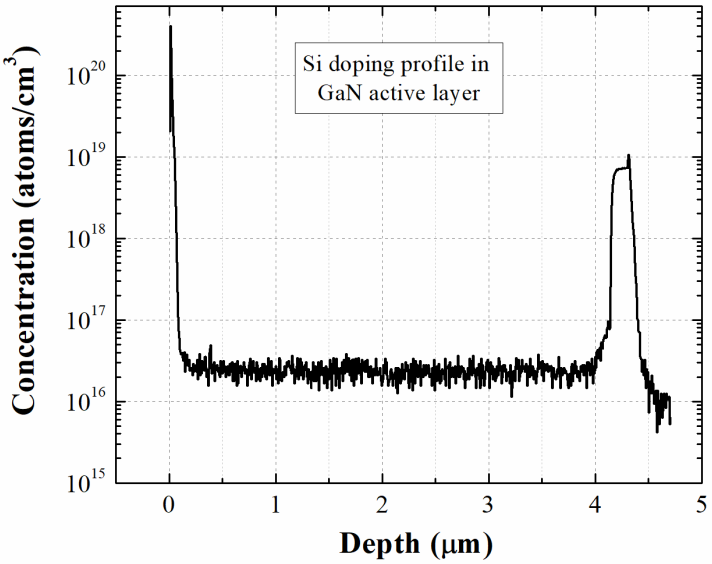

Fig. 4. The Si doping concentration distribution in GaN active layer identified from SIMS measurements.

The CL images obtained with the two different Ni frames namely L46C36 and L47C36 are depicted in Figs. 5(a) and 5(b). The outer blue circles in Fig. 5 represent the active area of the diodes [2]. The dark spots in the CL image indicate the physical location of the dislocations in the GaN epilayer [2,15]. The dislocations are inhomogeneously (randomly) distributed across the GaN active layer and they are agglomerated (known as dislocation clusters) at some specific locations, as denoted by the arrow in Fig. 5. It is identified from the CL imaging of L46C36 and L47C36 that the large-sized (200 µm) diodes consist of more dislocations as compared to the 100 µm SBDs. Part of the dislocations may not be detected by the CL imaging owing to the chosen luminescence contrast and

the lack of resolution [2].

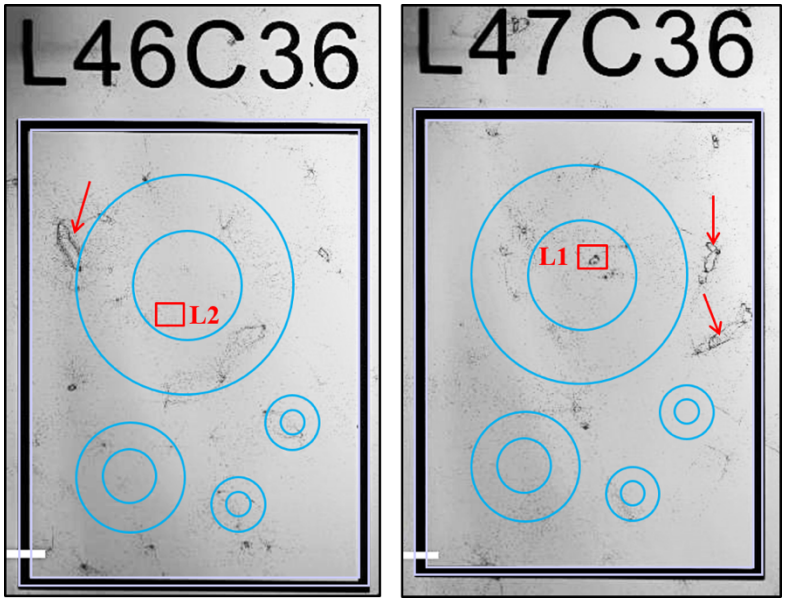

Fig. 5. Cathodoluminescence (CL) images obtained with two different Ni frames (a) L46C36 and (b) L47C36.

The Raman spectra of the n-type GaN epilayer acquired at RT in backscattering geometry mode are plotted in Fig. 6. Note that, Renishaw inVia Confocal Raman microscope [13] is specifically designed for the purpose of minimizing the superposition of phonon modes arriving from the substrate and the depth inhomogeneities, therefore it is considered that the major contribution of the spectra arises from the GaN epilayer due to the Raman scattering phenomena [19]. The commonly observed hexagonal bulk GaN phonon modes [4,15,19-21] such as E_2 (high) at 567.2 ± 0.1 cm^{-1} and A_1 (LO) at 733.4 ± 0.1 cm^{-1} are detected in the Raman spectra, along with the E_1 (TO) peak at ~558 cm^{-1} seen at the low-frequency side of E_2 (high) [4,19]. The spectral counts are normalized according to the intensity of the E_2 (high) phonon mode. It is noted that the Raman shift values for E_2 (high) and A_1 (LO) modes are consistent with the literature data [4,15,19-21]. The narrow full-width-half-maximum (FWHM) of 3.5 ± 0.1 cm^{-1} of the E_2 (high) peak reveals the crystalline quality and homogeneity of the n-type GaN epilayer [15,20]. The E_1 (TO) phonon mode is generally not active in this backscattering geometry along the c-axis. So, the existence of crystal defects in the epilayer (refer to Fig. 5) may induce a weak appearance of the E_1 (TO) peak in the Raman spectra, referring to the work of Huang *et al.* [19].

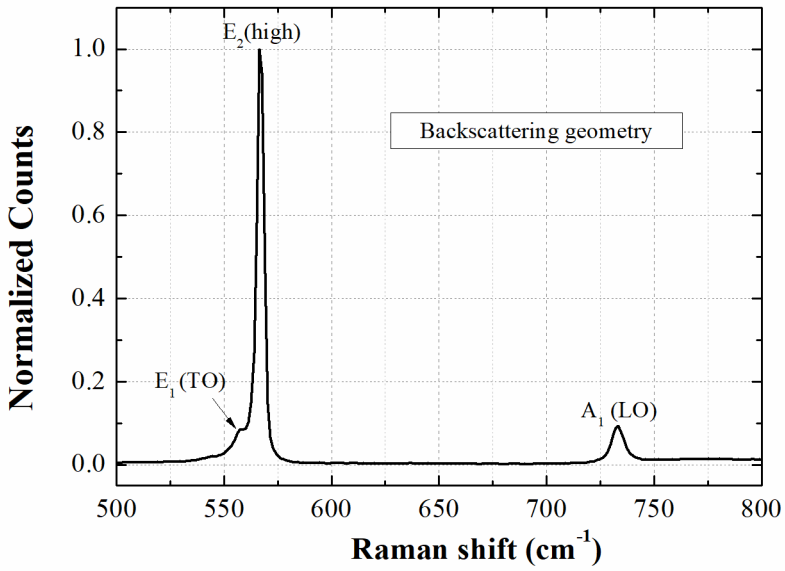

Fig. 6. Raman spectra of the n-type GaN epilayer acquired at RT in backscattering geometry.

The Raman volume (3D) mapping images are constructed after the mixed Gaussian-Lorentzian curve fitting analysis of the phonon modes. The E_2 (high) position can be used to probe the biaxial stress (σ_{xx}) in the epilayer as per the equation $\Delta\omega = K\sigma_{xx}$, where $\Delta\omega$ is the phonon frequency shift of the E_2 (high) Raman mode, and K is the linear stress coefficient with a value between 3 to 4 cm^{-1}/GPa, based on the literature reports [20,21]. Figure 7 illustrates (a) top view and (b) bottom view of the Raman volume mapping for E_2 (high) position, measured at the designated location L1 in the L47C36 frame. The 3D volume mapping has been acquired for the entire epilayer depth of 5 µm. Note that, the location L1 in the frame L47C36 contains considerable dislocations in the mapping region (refer to Fig. 5). It is shown in Fig. 7 that the E_2 (high) Raman shift slightly increases (0.5 cm^{-1} in range) along with the vertically downward direction may be due to compressive stress in the epilayer [20-22]. Since the GaN active layer is lattice-matched (and absence of TCE mismatching) with the homoepitaxial GaN substrate, the small compressive stress (up to 0.5 cm^{-1}) existing in the epilayer could be attributed to the defects and dislocations in the active volume. The red-colored regions (compressive stress) in the E_2 position Raman mapping may correspond to the dislocation clusters, based on the E_2 Raman mapping observations of Kokubo *et al.* [23]. The top and bottom views of the Raman volume mapping for the E_2 (high) position, attained at the selected epilayer location "L2" in the L46C36 frame are displayed in Figs. 8(a) and 8(b). Yet again, a small increase in the E_2 (high) Raman shift (~ 0.5 cm^{-1}) is noticed along with the depth possibly because of the compressive stress induced by the defects. The CL images (Fig. 5) show that the epilayer location L2 in the frame L46C36 comprises relatively lower dislocations than the L1 in L47C36. Accordingly, the red-colored regions (dislocations) in the Raman mapping are mostly observed in the lower part of the epitaxial layer, which may be originated from the extended defects in the substrate. The surface of the samples

appears in blue at both L1 and L2, this can be attributed to either a fitting artifact caused by the de-focalization or tensile stress at the surface. Nevertheless, the variation in the E_2 (high) position is found to be minimal (only in the 0.5 cm^{-1} range) at all the locations analyzed in this work. Therefore the E_2 Raman volume mapping shows the rather stress-free homoepitaxial GaN samples.

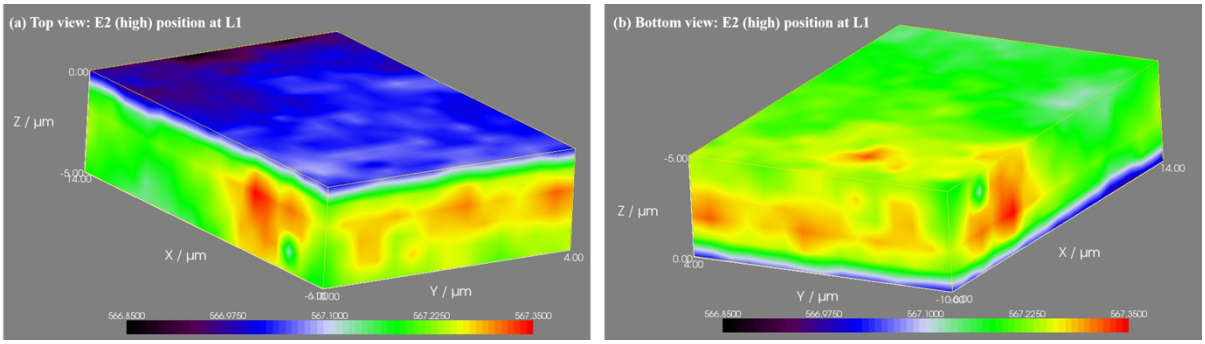

Fig. 7. (a) Top view and (b) Bottom view of the E_2 (high) position Raman volume mapping, acquired at the designated epilayer location "L1" in the L47C36 frame.

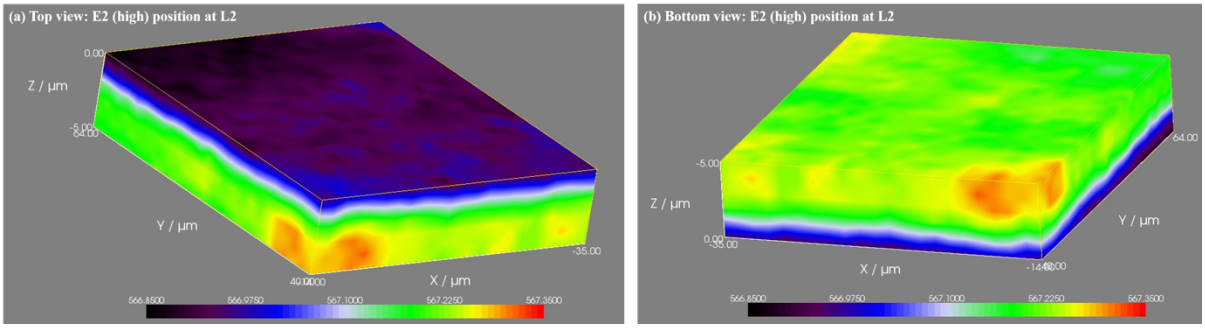

Fig. 8. (a) Top view and (b) Bottom view of the E_2 (high) position Raman volume mapping, attained at the selected epilayer location "L2" in the L46C36 frame.

3.2. Electrical Characteristics

Figure 9(a) shows the measured forward current density (J_F-V_F) characteristics (in semi-log scale) of the large (d = 200 µm), medium (d = 100 µm), and small (d = 50 µm) sized SBDs in the frame L47C36 at 293 K. Almost the same forward current density (J_F) is noticed in all the diodes, so J_F is independent of the diode active area; this indicates that the edge leakage current [24] at the contact periphery is negligible in the Ni/GaN SBDs [2]. The fitting analysis of the measured J_F-V_F curves is carried out to identify the forward current transport process in the SBDs. Figure 9(b) demonstrates that the forward J_F-V_F (at 293 K and 373 K) of the SBD entirely follows the standard thermionic emission (TE) model [11,24-26], through the emission of electrons from the semiconductor to the metal over the potential barrier:

$$J_{TE} = J_s \exp\left(\frac{q(V - IR_s)}{nkT} - 1\right) \tag{1}$$

$$J_s = A^* T^2 \exp\left(-\frac{q\Phi_B}{kT}\right) \tag{2}$$

where J_s is the saturation current density, q is the elementary charge, V is the applied bias voltage, I is the resultant current, R_s is the series resistance, k is the Boltzmann constant, T is the temperature, A^* is the Richardson's constant for GaN (26.9 $Acm^{-2}K^{-2}$ [2,10]), n is the ideality factor, Φ_B is the Schottky barrier height (SBH). The TE model fitting of J_F-V_F yields near-unity ideality factor (n = 1.1-1.12), promising SBH value (Φ_B = 0.81-0.83 eV) and low series resistance (R_s = 5.3-5.6 Ω) for all measured vertical GaN SBDs. It is identified that the SBD parameters (n, Φ_B, and R_s) extracted from the Cheung's method [27] are also consistent with the TE model evaluation of J_F-V_F. The turn-on voltage (V_{on} = 0.56-0.58 V) of the SBDs is determined by the linear interpolation [6] of the J_F-V_F plot. All the parasitic leakage currents [8,24,26] responsible for non-ideal diode behavior are absent in the Ni/GaN SBDs, even at low bias voltages (V_F < 0.3 V). Indeed, the standard TE theory essentially governs the forward current of the SBDs in the temperature range of 293 K to 393 K. Hence, J_F-V_F of the vertical Ni/GaN SBDs has shown quasi-ideal forward current characteristics.

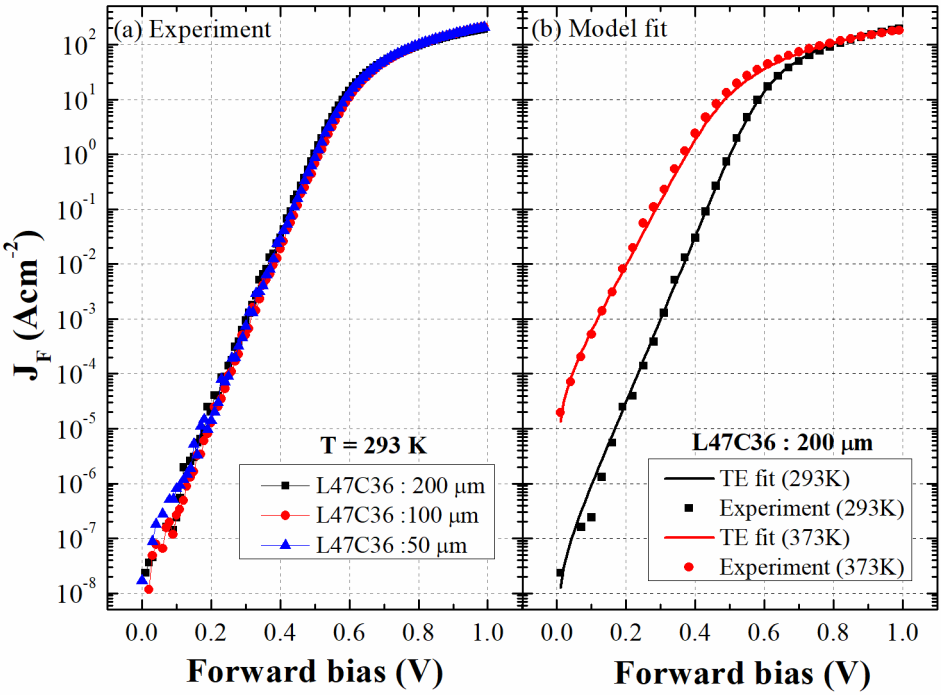

Fig. 9. (a) Measured forward current density (J_F-V_F) characteristics (in semi-log scale) of the large (d = 200µm), medium (d = 100 µm) and small (d = 50 µm) sized SBDs in the frame L47C36 at 293 K. (b) The curve fitting analysis shows that J_F-V_F properties of the SBD entirely follow the standard thermionic emission theory at 293K and 373 K.

Figure 10 illustrates the comparison of reverse current density (J_R-V_R) properties of the large diameter (200 µm) diodes with the medium-sized (100 µm) SBDs in the frames L46C36 and L47C36 at 293 K. No breakdown is observed up to V_R = -200 V from the J_R-V_R characteristics of the SBDs (i.e. V_{BR} < -200V). The reverse J_R-V_R characteristics of the 200 µm diodes in both frames (L46C36 and L47C36) are nearly identical. Similarly, both 100 µm diodes exhibit almost the same J_R-V_R. One

peculiar observation in Fig. 10, the leakage current density of the 100 µm diodes is slightly higher than the large-diameter SBDs up to V_R = -110 V. But at V_R = -125 V, all the diodes exhibit approximately the same reverse current density of J_R = ~8×10^{-6} Acm^{-2}. Thereafter (beyond V_R = -150 V), the 100 µm diodes have shown relatively lower leakage current than its counterpart. Hence, dissimilar J_R-V_R characteristics are noticed between the 200 µm and the 100 µm diodes in the same frame. Referring to the CL images in Fig. 5, it is stated that the inhomogeneous distribution of defects across the epilayer may be the reason for the observed discrepancy in the leakage current between the 200 µm and the 100 µm diodes in the same frame.

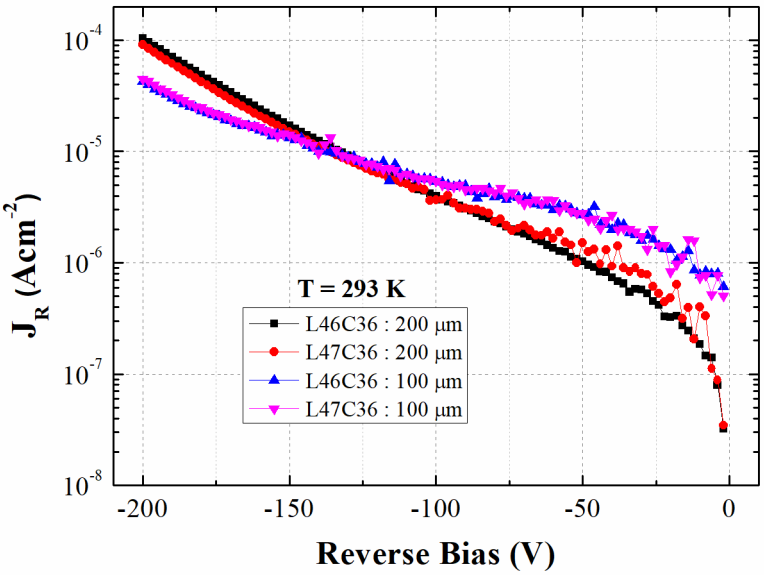

Fig. 10. The semi-log reverse current density (J_R-V_R) properties of the large diameter (200 µm) diodes are compared with the medium-sized (100 µm) SBDs in the frames L46C36 and L47C36 at 293 K.

The various current transport mechanisms contributing to the leakage current of the 200 µm diodes are identified by fitting the measured J_R-V_R and are plotted in Fig. 11(a). A notable reverse current flows through the emission of electrons from the metal to the semiconductor over top of the barrier, due to the Schottky barrier lowering (SBL) effect [25] caused by the voltage-dependent electric field. The reverse current density produced due to the SBL effect (J_{SBL}) is given by [10,25]

$$J_{SBL} = A^* T^2 \exp\left(-\frac{q(\Phi_B - \Delta\Phi)}{kT}\right) \tag{3}$$

$$\Delta\Phi = \sqrt{\frac{qE_m}{4\pi\varepsilon_s}} \tag{4}$$

where $\Delta\Phi$ is the reduced Schottky barrier height due to SBL effect, ε_s is the dielectric constant of GaN (8.9 ε_0), and E_m is the peak electric field existing at the Ni/GaN Schottky interface [25,26]:

$$E_m = \sqrt{\frac{2qN_D(V_{bi} + V_R)}{\varepsilon_s}} \tag{5}$$

where N_D represents the net doping concentration in the epilayer and V_{bi} is the built-in potential of the SBD. The thermionic field emission (TFE) component induces a significant leakage current in the SBD, due to the tunneling of thermally excited electrons from the metal to the semiconductor through the Schottky barrier. The reverse current conduction due to the TFE (J_{TFE}) can be expressed as [9,28]

$$J_{TFE} = \frac{A^* T q \hbar E_m}{k} \sqrt{\frac{\pi}{2 m_e k T}} \exp\left[-\frac{1}{kT} \left(\Phi_B - \frac{(q\hbar E_m)^2}{24 m_e (kT)^2} \right) \right] \quad (6)$$

where $\hbar$ is the reduced Planck constant, m_e is the effective mass of electron in GaN (0.23 m_0). Suda *et al.* [9] and Ren *at al.* [10] also identified that the TFE current contribution is significant during the reverse bias operation of the nearly-ideal vertical GaN-on-GaN SBDs. It is found that the Fowler-Nordheim tunneling (FNT) current provides a contribution to the reverse leakage current at higher reverse bias voltages (V_R > -125 V for 200 µm diodes), due to the triangular barrier formation. The FNT current essentially dominates the leakage current beyond -150 V. The FNT current density (J_{FNT}) due to the penetration of electrons along with the metal Fermi level to the semiconductor through the barrier can be represented by [24,25]

$$J_{FNT} = A E_m^2 \exp\left(-\frac{B}{E_m} \right) \quad (7)$$

$$B = \frac{8\pi \sqrt{2 m_e (q\Phi_B)^3}}{3qh} \quad (8)$$

where A is a constant, and h is the Planck constant. In large diameter (200 µm) diodes, J_{SBL} and J_{TFE} are mainly responsible for the reverse conduction current up to -150 V, and at higher electric fields the J_{FNT} contribution plays a major role in deciding the J_R-V_R characteristics, as perceived from Fig. 11(a). The total reverse current density (J_T) is computed by adding all these current transport components together in the model ($J_T = J_{SBL}+J_{TFE}+J_{FNT}$) [24]. The computed J_T from the model fitting has given a good agreement with the measured J_R-V_R, as shown in Fig. 11(a). The schematic diagram of fundamental current transport mechanisms involved in the forward and reverse bias operation of the vertical Ni/GaN SBDs is illustrated in Figs. 12(a) and (b).

The reverse current conduction mechanisms contributing to the leakage current of the medium-sized (100 µm) diodes are plotted in Fig. 11(b). It is clearly shown that J_{SBL} primarily governs the J_R-V_R properties up to V_R = -150 V and the J_{FNT} controls the leakage current at higher reverse voltages (V_R > -175 V). The J_R-V_R characteristics of the 100 µm diodes are effectively fitted based on the expression of $J_T = J_{SBL}+J_{FNT}$; thus the reverse J_R-V_R fitting of the 100 µm diode is accomplished without considering J_{TFE} in the model. Similar observations are noticed in the small-sized (50 µm) diodes (not shown).

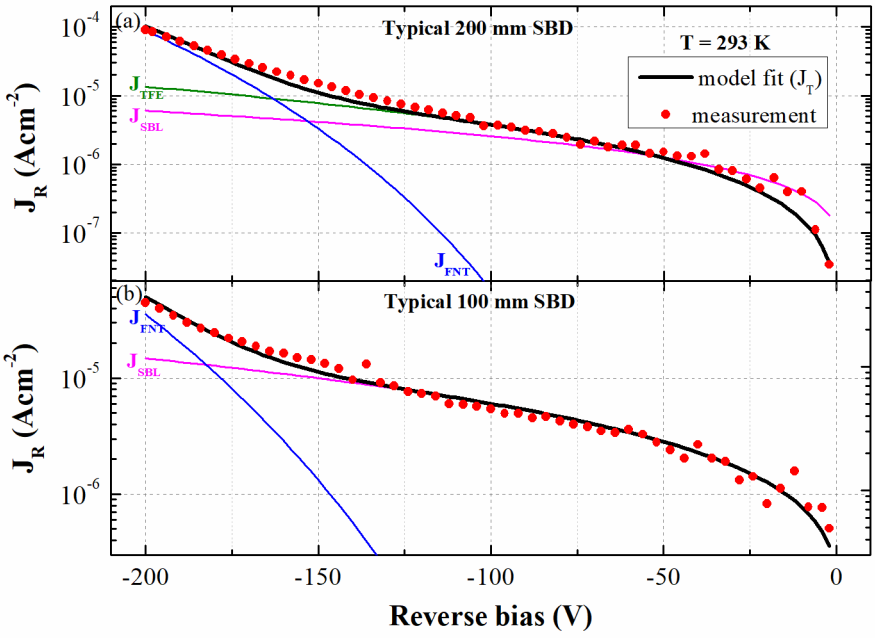

Fig. 11. The various leakage current transport mechanisms identified in typical (a) large-diameter (200 µm) and (b) medium-sized (100 µm) diodes are analyzed by fitting the measured J_R-V_R characteristics at 293 K.

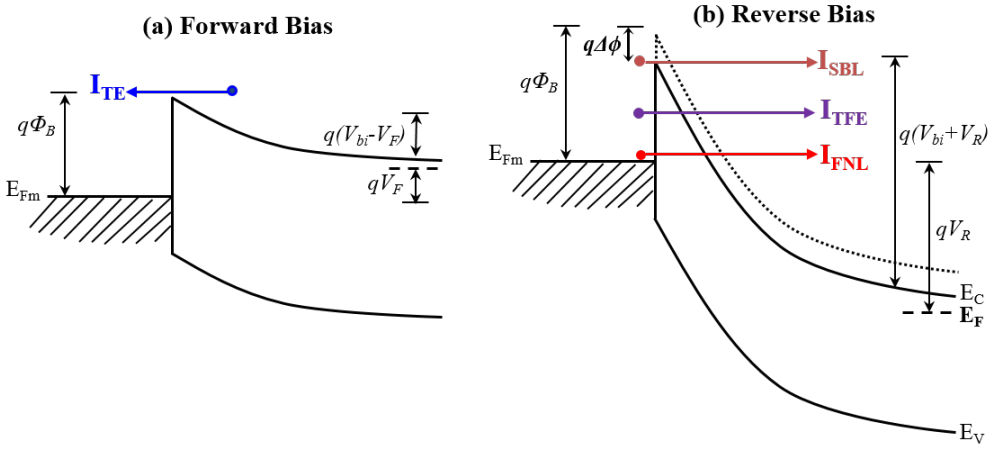

Fig. 12. Schematic illustration of (a) TE during forward bias mode and (b) three fundamental current transport process (SBL, TFE and FNT) involved in the reverse bias operation of the vertical Ni/GaN-on-GaN SBDs.

The J_F-V_F characteristics of the Ni/GaN SBDs measured at different temperatures ranging from 293 K to 373 K are plotted in Fig. 13(a). The temperature-induced changes in the series resistance (R_s) of the SBDs are displayed in the inset of Fig. 13(a). The turn-on voltage is found to decrease (V_{on} = 0.56 V at 293 K, 0.5 V at 243 K, and 0.43 V at 373 K, as extracted by linear interpolation) with the increasing temperature due to the associated reduction in the diode built-in potential. The observed current drop in the linear region is due to the increase in the series resistance (R_s = 5.35 Ω at 293K, and 8 Ω at 373 K). The temperature-dependent J_R-V_R characteristics are shown in Fig. 13(b). It is seen that the leakage current density rapidly increases with the temperature, due to the corresponding upsurge in the J_{SBL} and J_{TFE} components, as identified from the curve fitting analysis. From T = 333

K, the leakage current density at -100 V (J_R = 4.28×10^{-5} Acm^{-2} at 333 K, 1.97×10^{-4} Acm^{-2} at 353 K, and 6.88×10^{-4} Acm^{-2} at 373 K) is roughly increased by a numerical value of four at every 20 K rise in the temperature.

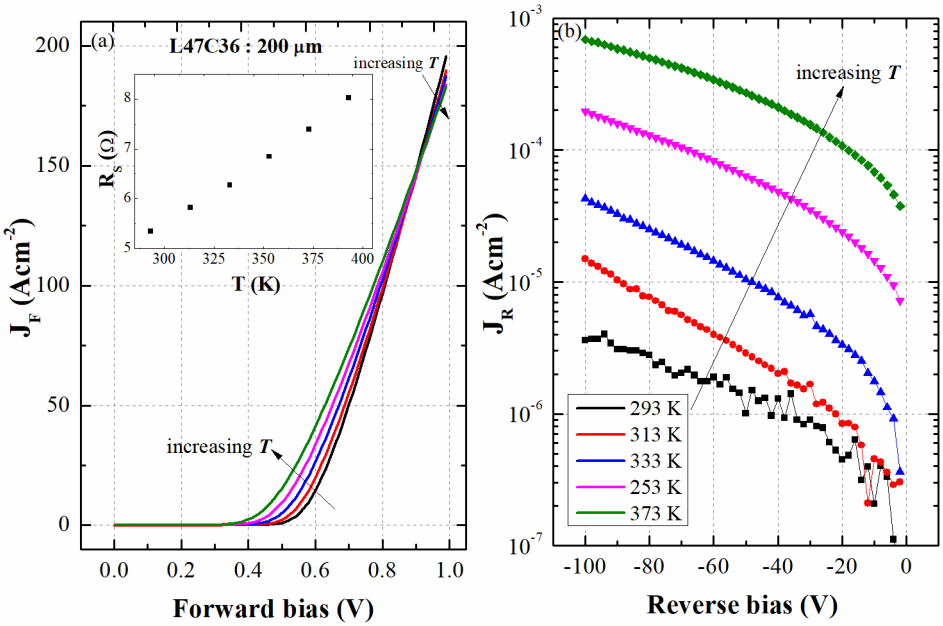

Fig. 13. (a) J_F-V_F and (b) J_R-V_R characteristics of the vertical Ni/GaN SBDs measured at different temperatures ranging from 293 K to 373 K. The temperature-induced changes in the series resistance (R_s) are displayed in the inset of Fig. 12(a).

Figure 14(a) shows the temperature (from 293 K to 393 K) induced changes in the SBH (Φ_B) and ideality factor (n) computed using the TE model Eqn. (1). A small reduction in the SBH is observed with the increase in the temperature (0.82 eV at 293 K, and 0.79 eV at 393 K), as similar to the work of Maeda *et al.* [11]. On the other hand, a slight increase in the ideality factor is noted with the increasing temperature. Maeda *et al.* [11] detected a decrease in the ideality factor (1.1-1.01) when the temperature is increased from 200 K to 300 K; beyond that the ideality factor is close to unity for the wide temperature range of 300 K to 600 K. Nevertheless, we found that the temperature effect on the ideality factor is found to be minimal (1.11 at 293 K, and 1.21 at 393 K) in the SBDs. Roccaforte *et al*. [5] reported that the non-ideal GaN SBD could exhibit an increase in the SBH and a decrease in the ideality factor with the increasing temperature, and the non-ideal diode often displays a strong temperature dependence. Since the TE model essentially governs the forward current transport up to T = 393 K, the SBH and ideality factor have shown a weak temperature dependence in this work. Therefore, quasi-ideal diode characteristics have been obtained [11] with the vertical Ni/GaN-on-GaN SBDs. Conventional $ln(J_s/T^2)$ vs. q/kT Richardson plot is constructed from the J_F-V_F-T properties and is depicted in Fig. 14(b). The effective Schottky barrier height of Φ_{eff} = ~0.9 eV is computed from the slope of the Richardson plot, according to the rearranged Eqn. (2) [14,25]

$$\ln\left(\frac{J_S}{T^2}\right) = -\frac{q}{kT}\Phi_{eff} + \ln(A^*) \quad (9)$$

Since the Richardson method reflects the typical behavior of the diode at various temperatures [5,25], the effective SBH (Φ_{eff} = ~0.9 eV) calculated from the Richardson plot is normally higher than the SBH estimated using the TE model (Φ_B = ~0.82 V) at room temperature.

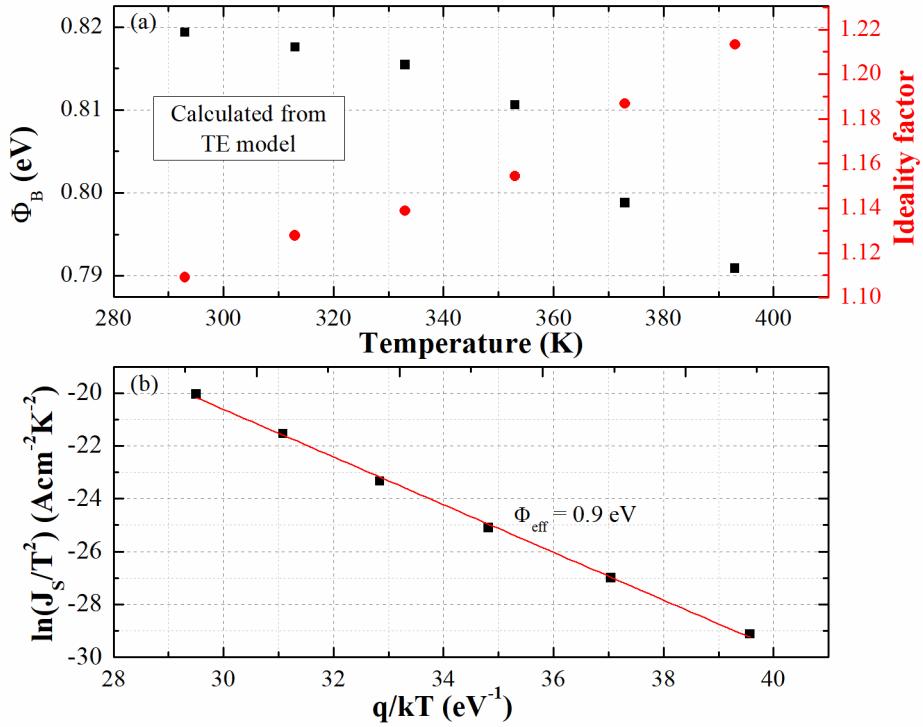

Fig. 14. (a) The weak temperature dependence (293 K to 393 K) of the SBH (0.82 eV to 0.79 eV) and ideality factor (1.1 to 1.2) identified from the TE model. (b) Conventional $ln(J_s/T^2)$ vs. q/kT Richardson plot yields the effective SBH of Φ_{eff} = ~0.9 eV.

3.3. Interface States and Deep-level Traps

In most of the practical Schottky contacts, a thin interfacial layer may exist in between the metal/semiconductor interface. It is a challenging task in fabrication to obtain an intimate contact, devoid of an interfacial oxide layer [25,26]. In general, the interfacial layer thickness is relatively small such that this layer is transparent to the electrons [25,26]. About 3 nm of the interfacial layer has been formed at the surface of the air-exposed GaN layer [29]. Therefore, the interface state density (N_{SS}) equilibrium with the GaN material is calculated from the forward I_F-V_F properties of the SBD. For this estimation, it is assumed that the SBH and the ideality factor are bias-dependent parameters. The bias-dependent SBH $\Phi_B(V_F)$ in the forward bias region can be expressed as [29-31]

$$\Phi_B(V_F) = \Phi_B + \left(1 - \frac{1}{n(V_F)}\right)V_f \quad (10)$$

where $V_f = V - IR_s$ [31], and $n(V_F)$ denotes the bias-dependent ideality factor during the forward bias operation, as given by

$$n(V_F) = \frac{qV_f}{kT\ln(I_F / I_S)} \tag{11}$$

where I_S represents the saturation current and I_F is the forward current. The interface state density (N_{SS}) in equilibrium with the GaN semiconductor is calculated by [29,30]

$$N_{SS} = \frac{1}{q}\left(\frac{\varepsilon_i}{\delta}(n(V_F)-1) - \frac{\varepsilon_s}{W_D}\right) \tag{12}$$

where W_D denotes the depletion-region thickness, δ symbolizes the interfacial layer thickness, ε_i signifies the dielectric constant of the interfacial layer. The interfacial layer thickness is chosen as 3nm based on the work of Ahaitouf *et al.* [29]. The energy distribution of the interface states (E_{SS}) located below the conduction band (E_C) edge (in n-type material) can be determined by

$$E_C - E_{SS} = q[\Phi_B(V_F) - V_f] \tag{13}$$

Figure 15 shows the interface state density (N_{SS}) distribution located below the conduction band edge (E_C - E_{SS}) for the 200 µm diodes in the frames L46C36 and L47C36 (at 293 K). The interface state density is almost constant (N_{SS} = ~9×10^{11} eV^{-1} cm^{-2}) in the energy range of E_C - 0.23 eV to E_C – 0.5 eV. After that, N_{SS} exponentially rises and reaches the maximum value (N_{SS} = 4.9 $\times10^{12}$ eV^{-1} cm^{-2}) at E_C – 0.74 eV. It is realized that both diodes (in L46C36 and L47C36) have a low interface state density (N_{SS} < 5×10^{12} eV^{-1} cm^{-2}) at Ni/GaN Schottky contact, as compared to N_{SS} (> 10^{13} eV^{-1} cm^{-2}) reported by Ahaitouf *et al.* [29]. This result confirms the Ni/GaN Schottky interface quality of our vertical GaN-on-GaN SBDs.

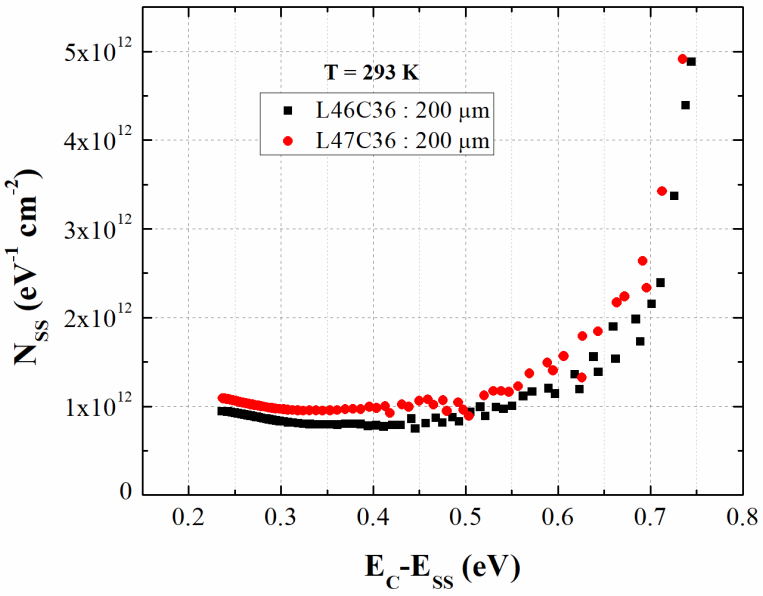

Fig. 15. The interface state density (N_{SS}) distribution located below the conduction band edge (E_C-E_{SS}) of the 200 µm diodes in the frames L46C36 and L47C36 (at 293 K).

Deep-level transient Fourier spectroscopy (DLTFS) was used to identify the electrically active defects (deep-level traps) present in the GaN active layer of the SBD. Figure 16 shows the DLTFS spectra acquired (with the quiescent reverse bias V_R = -10 V) with the 200 µm diodes in the frames L46C36 and L47C36 for the temperatures ranging from 50 K to 400 K. The first order Fourier sine coefficient b_1 [12,14] is chosen to represent the DLTFS signal. A strong DLTFS peak T2 at ~265 K is detected, together with the appearance of a small peak T1 at ~127 K. Note that, the positive DLTFS peak in our measurement setup corresponds to the electron trap located below the conduction band ($E_C - E_T$) [14]. In the direct extraction mode, the emission time constant (τ_n) of each exponential transient (recorded during thermal ramp-up) is internally computed by the discrete Fourier transformation and the Arrhenius plots are constructed for T1 and T2 as per the following expression [14,32]

$$\ln\left(\tau_n T^2\right) = \frac{E_a}{kT} - \ln\left(\frac{\sigma_n N_C v_{th}}{g T^2}\right) \tag{14}$$

where E_a is the trap activation energy, σ_n is the capture cross-section of the trap, v_{th} is the carrier thermal velocity, N_C is the effective density of states in the conduction band, and g is the degeneracy factor. The Arrhenius plots for the traps T1 and T2 identified in the diodes located in the frames L46C36 and L47C36 are given in Fig. 17. For the diode in L46C36, the trap T2 signatures E_{T2} = E_C - 0.55 eV and σ_{n2} = 10^{-15} cm^2 are determined from the slope and intercept of the Arrhenius plot according to the Eqn. (15). Similar trap T2 parameters (E_{T2} = E_C - 0.56 eV and σ_{n2} = 1.15×10^{-15} cm^2) are attained for the diode in L47C36. The trap concentration (N_T) is calculated from the amplitude of the DLTFS signal (ΔC) based on the following equation [14,33]

$$N_T \approx 2N_D \frac{\Delta C}{C_R} \tag{15}$$

where C_R is the reverse bias capacitance (at V_R = -10 V). The trap density of T2 for the diodes in the frames L46C36 and L47C37 are found to be N_{T2} = 1×10^{15} cm^{-3}, and 1.1×10^{15} cm^{-3}, respectively. The trap parameters calculated for T1 are E_{T1} = E_C - 0.18 eV, σ_{n1} = ~1.3×10^{-18} cm^2, and N_{T1} = 4×10^{13} cm^{-3}. Therefore, nearly the same trap levels at E_C - 0.18 eV (T1) and E_C - 0.56 eV (T2) are detected in both diodes (L46C36 and L47C36), revealing that these trap states are omnipresent defects in the GaN epilayer. The possible physical origin of the trap T1 at E_C - 0.18 eV is the nitrogen-vacancy (V_N) [34,35]. The deep-level trap T2 at E_C - 0.56 eV can be attributed to the nitrogen antisite (N_{Ga})-related defect [36,37] in the n-type homoepitaxial GaN layer.

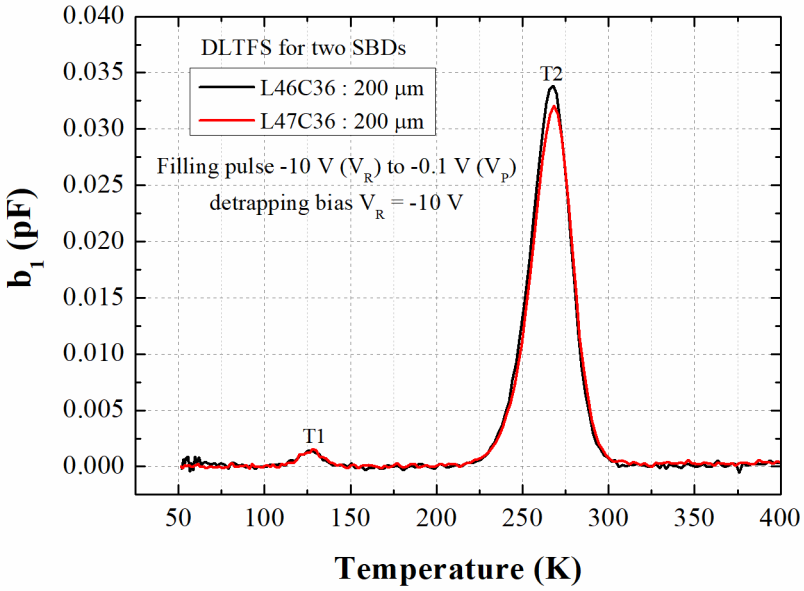

Fig. 16. Deep-level transient Fourier spectroscopy (DLTFS) acquired with the 200 µm diodes in the frames L46C36 and L47C36 for the temperatures ranging from 50 K to 400 K.

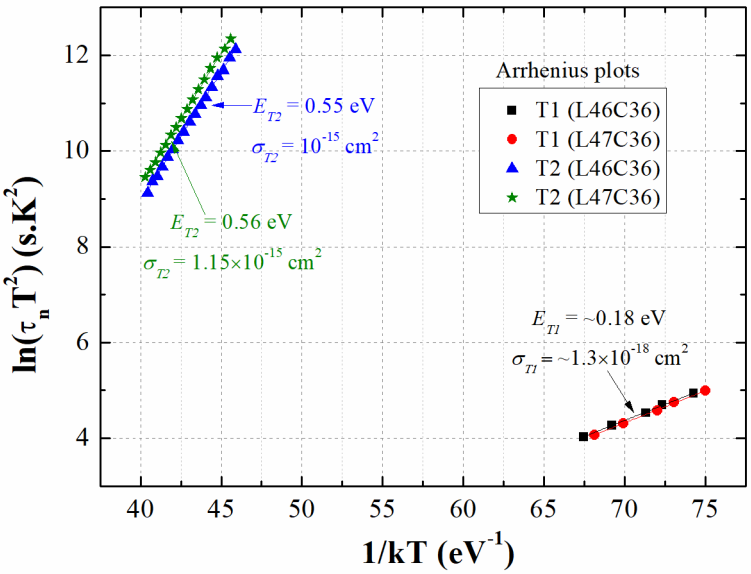

Fig. 17. Arrhenius plots for the traps T1 and T2 identified in the diodes located in the frames L46C36 and L47C36.

Figure 18 depicts the energy band diagram of the Ni/GaN SBD with a thin interfacial layer (δ) under thermal equilibrium. The energy distribution (E_C - E_{SS}) of the interface state density (N_{SS}) at the Ni/GaN interface is illustrated in Fig. 18, along with the energy position of the epilayer traps T1 at E_C – 0.18 eV and T2 at E_C – 0.56 eV.

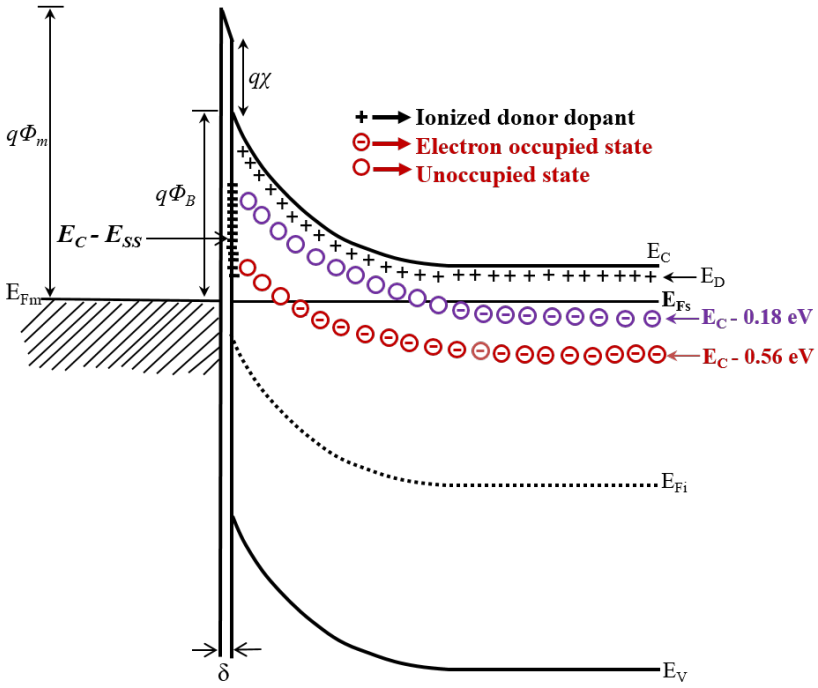

Fig. 18. The energy band diagram of Ni/GaN SBD with a thin interfacial layer (δ) under thermal equilibrium condition shows the energy distribution (E_C - E_{SS}) of the interface state density (N_{SS}) and the energy position of the epilayer traps T1 at E_C – 0.18 eV and T2 at E_C – 0.56 eV.

4. Conclusion

The comprehensive characterization studies are carried to demonstrate the quasi-ideal Schottky behaviour of the vertical GaN-on-GaN SBDs. The AFM and µ-Raman investigations reveal the good crystalline quality of the epilayer (almost stress-free) and the smooth surface with 0.16 nm RMS. The CL imaging suggests that the dislocations are randomly distributed across the epilayer. The Si-doping concentration (~2.5×10^{16} cm^{-3}) in the epilayer is identified from the SIMS. The GaN SBDs have shown nearly-ideal n = 1.1, promising SBH (0.82 eV), low V_{on} = 0.56 V, $J_R < 5.5\times10^{-6}$ Acm^{-2} at V_R = -100 V, V_{BR} < -200 V, and lower $N_{SS} < 5\times10^{12}$ eV^{-1} cm^{-2} at the Ni/GaN interface. The standard TE theory entirely governs the forward current density in the temperature range of 293 K - 393 K, as a result a weak temperature dependence of Φ_B and n is obtained; thus the quasi-ideal SBD characteristics are demonstrated. The SBL effect and TFE mechanisms are responsible for the reverse current transport process up to -150 V, and the FNT current primarily controls the J_R-V_R beyond -150 V due to the triangular barrier formation. Moreover, the same trap parameters at E_C – 0.18 eV and E_C – 0.56 eV are identified for the diodes located in different regions, therefore these traps are omnipresent defects in the n-type GaN epilayer.

Acknowledgement

The results were obtained during P. V. Raja's postdoc at Ampere Laboratory. His postdoc is financially supported by IPCEI (Important Projects of Common European Interest) on Microelectronics / Nano 2022. This work was supported by the technology facility network

RENATECH and the French National Research Agency (ANR) through the project C-PI-GaN (ANR-18-CE05-0045) and the “Investissements d’Avenir” program GaNeX (ANR-11-LABX-0014).

References

[1] W. Li, K. Nomoto, K. Lee, S. M. Islam, Z. Hu, M. Zhu, X. Gao, M. Pilla, D. Jena, H. G. Xing, Development of GaN vertical trench-MOSFET with MBE regrown channel, IEEE Trans. Electron Devices. 65 (2018) 2558-2264. https://doi.org/10.1109/TED.2018.2829125.

[2] T. H. Ngo, R. Comyn, E. Frayssinet, H. Chauveau, S. Chenot, B. Damilano, F. Tendille, B. Beaumont, J. P. Faurie, N. Nahas, Y. Cordier, Cathodoluminescence and electrical study of vertical GaN-on-GaN Schottky diodes with dislocation clusters, J. Cryst. Growth 552 (2020) 125911. https://doi.org/10.1016/j.jcrysgro.2020.125911.

[3] L. Sang, B. Ren, M. Sumiya, M. Liao, Y. Koide, A. Tanaka, Y. Cho, Y. Harada, T. Nabatame, T. Sekiguchi, S. Usami, Initial leakage current paths in the vertical-type GaN-on-GaN Schottky barrier diodes, Appl. Phys. Lett. 111 (2017) 122102. https://doi.org/10.1063/1.4994627.

[4] A. J. Eric N’Dohi, C. Sonneville, L. V. Phung, T. H. Ngo, P. D. Mierry, E. Frayssinet, H. Maher, J. Tasselli, K. Isoird, F. Morancho, Y. Cordier, D. Planson, Micro-Raman characterization of homo-epitaxial n doped GaN layers for vertical device applications, AIP Adv. 12 (2022) 025126. https://doi.org/10.1063/5.0082860.

[5] F. Roccaforte, F. Giannazzo, A. Alberti, M. Spera, M. Cannas, I. Cora, B. Pécz, F. Iucolano, and G. Greco, Barrier inhomogeneity in vertical Schottky diodes on free standing gallium nitride, Mater. Sci. Semicond. Process. 94 (2019)164-70. https://doi.org/10.1016/j.mssp.2019.01.036.

[6] K. Fu, H. Fu, X. Huang, T.-H. Yang, C.-Y. Cheng, P. R. Peri, H. Chen, J. Montes, C. Yang, J. Zhou, X. Deng, Reverse leakage analysis for as-grown and regrown vertical GaN-on-GaN Schottky barrier diodes, IEEE J. Electron Devices Soc. 8 (2020) 74-83. https://doi.org/10.1109/JEDS.2020.2963902.

[7] X. Guo, Y. Zhong, X. Chen, Y. Zhou, S. Su, S. Yan, J. Liu, X. Sun, Q. Sun, and H. Yang, Reverse leakage and breakdown mechanisms of vertical GaN-on-Si Schottky barrier diodes with and without implanted termination, Appl. Phys. Lett. 118 (2021) 243501. https://doi.org/10.1063/5.0049706.

[8] L. Chen, N. Jin, D. Yan, Y. Cao, L. Zhao, H. Liang, B. Liu, E. X. Zhang, X. Gu, R. D. Schrimpf, D. M. Fleetwood, Charge transport in vertical GaN Schottky barrier diodes: a refined physical model for conductive dislocations, IEEE Trans. Electron Devices 67 (2020) 841-846.

[9] J. Suda, K. Yamaji, Y. Hayashi, T. Kimoto, K. Shimoyama, H. Namita, and S. Nagao, Nearly ideal current-voltage characteristics of Schottky barrier diodes formed on hydride-vapor-phase-epitaxy-grown GaN free-standing substrates, Appl. Phys. Express 3 (2010) 101003. https://doi.org/10.1143/APEX.3.101003.

[10] B. Ren, M. Liao, M. Sumiya, L. Wang, Y. Koide, and L. Sang, Nearly ideal vertical GaN Schottky barrier diodes with ultralow turn-on voltage and on-resistance, Appl. Phys. Express 10 (2017) 051001. https://doi.org/10.7567/APEX.10.051001.

[11] T. Maeda, M. Okada, M. Ueno, Y. Yamamoto, T. Kimoto, M. Horita, and J. Suda, Temperature dependence of barrier height in Ni/n-GaN Schottky barrier diode, Appl. Phys. Express 10 (2017) 051002. https://doi.org/10.7567/APEX.10.051002.

[12] S. Weiss, and R. Kassing, Deep level transient fourier spectroscopy (DLTFS) - a technique for the analysis of deep level properties, Solid-State Electron. 31 (1988) 1733-1742. https://doi.org/10.1016/0038-1101(88)90071-8.

[13] WiRE Training Module, Renishaw inVia^{TW} confocal Raman microscope, Gloucestershire GL12 8JR, United Kingdom, 2020.

[14] PhysTech FT-1030 DLTFS manual, PhysTech GmbH. Am Mühlbachbogen 55d, D-85368 Moosburg, Germany, 2014.

[15] H. Gu, C. Hu, J. Wang, Y. Lu, J.-P. Ao, F. Tian, Y. Zhang, M. Wang, X. Liu, K. Xu, Vertical GaN Schottky barrier diodes on Ge-doped free-standing GaN substrates, J. Alloys. Compd. 780 (2019) 476-481. https://doi.org/10.1016/j.jallcom.2018.12.014.

[16] M. A. Reshchikov, M. Vorobiov, O. Andrieiev, K. Ding, N. Izyumskaya, V. Avrutin, A. Usikov, H. Helava, Y. Makarov, Determination of the concentration of impurities in GaN from photoluminescence and secondary-ion mass spectrometry, Sci. Rep. 10 (2020) 1-7. https://doi.org/10.1038/s41598-020-59033-z.

[17] J. A. Freitas Jr, M. A. Mastro, E. R. Glaser, N. Y. Garces, S. K. Lee, J. H. Chung, D. K. Oh, and K. B. Shim, Structural and optical studies of thick freestanding GaN films deposited by hydride vapor phase epitaxy, J. Cryst. Growth 350 (2012) 27-32. https://doi.org/10.1016/j.jcrysgro.2011.12.017.

[18] J. A. Freitas Jr, W. J. Moore, B. V. Shanabrook, G. C. B. Braga, S. K. Lee, S. S. Park, J. Y. Han, D. D. Koleske, Donors in hydride-vapor-phase epitaxial GaN. J. Cryst. Growth 246 (2002) 307-14. https://doi.org/10.1016/S0022-0248(02)01755-4.

[19] Y. Huang, X. D. Chen, S. Fung, C. D. Beling, and C. C. Ling, Spatial characterization of a 2 in GaN wafer by raman spectroscopy and capacitance-voltage measurements, J. Phys. D Appl. Phys. 37 (2004) 2814-2818. https://doi.org/10.1088/0022-3727/37/20/007.

[20] M. Kuball, Raman spectroscopy of GaN, AlGaN and AlN for process and growth monitoring/control, Surf. Interface Anal. 31 (2001) 987-999. https://doi.org/10.1002/sia.1134.

[21] D. G. Zhao, S. J. Xu, M. H. Xie, S. Y. Tong, and H. Yang, Stress and its effect on optical properties of GaN epilayers grown on Si (111), 6H-SiC (0001), and c-plane sapphire, Appl. Phys. Lett. 83 (2003) 677-679. https://doi.org/10.1063/1.1592306.

[22] G. Nootz, A. Schulte, L. Chernyak, A. Osinsky, J. Jasinski, M. Benamara, and Z. L.-Weber, Correlations between spatially resolved Raman shifts and dislocation density in GaN films, Appl. Phys. Lett. 80 (2002)1355-1357. https://doi.org/10.1063/1.1449523.

[23] N. Kokubo, Y. Tsunooka, F. Fujie, J. Ohara, S. Onda, H. Yamada, M. Shimizu, S. Harada, M. Tagawa, and T. Ujihara, Nondestructive visualization of threading dislocations in GaN by micro raman mapping, Jpn. J. Appl. Phys. 58 (2019) SCCB06. https://doi.org/10.7567/1347-4065/ab0acf.

[24] J. Ren, D. Yan, G. Yang, F. Wang, S. Xiao, and X. Gu, Current transport mechanisms in lattice-matched Pt/Au-InAlN/GaN Schottky diodes, J. Appl. Phys. 117 (2015)154503. https://doi.org/10.1063/1.4917566.

[25] S. M. Sze, K. K. Ng, Physics of Semiconductor Devices, 3rd ed. New Jersey, USA: John Wiley & Sons, 2007.

[26] E. H. Rhoderick, Metal-semiconductor contacts, IEE Proc. 129 (1982) 1-14. https://doi.org/10.1049/ip-i-1.1982.0001.

[27] S. K. Cheung, and N. W. Cheung, Extraction of Schottky diode parameters from forward current-voltage characteristics, Appl. Phys. Lett. 49 (1986) 85-87. https://doi.org/10.1063/1.97359.

[28] T. Hatakeyama, and T. Shinohe, Reverse characteristics of a 4H-SiC Schottky barrier diode, Mater. Sci. Forum 389-293 (2002) 1169-1172. https://doi.org/10.4028/www.scientific.net/MSF.389-393.1169.

[29] A. Ahaitouf, H. Srour, S. O. S. Hamady, N. Fressengeas, A. Ougazzaden, and J.-P. Salvestrini, Interface state effects in GaN Schottky diodes, Thin. Solid. Films 522 (2012) 345-351. https://doi.org/10.1016/j.tsf.2012.08.029.

[30] P. V. Raja, N. V. L. N. Murty, Thermal annealing studies in epitaxial 4H-SiC Schottky barrier diodes over wide temperature range, Microelectron. Reliab. 87 (2018) 213-221. https://doi.org/10.1016/j.microrel.2018.06.021.

[31] M. Sochacki, A. Kolendo, J. Szmidt, and A. Werbowy, Properties of Pt/4H-SiC Schottky diodes with interfacial layer at elevated temperatures, Solid-State Electron. 49 (2005) 585-590. https://doi.org/10.1016/j.sse.2005.01.015.

[32] P. V. Raja, M. Bouslama, S. Sarkar, K. R. Pandurang, J.-C. Nallatamby, N. DasGupta, and A. Dasgupta, Deep-level traps in AlGaN/GaN-and AlInN/GaN-based HEMTs with different buffer doping technologies, IEEE Trans. Electron Devices 67 (2020) 2304-2310. https://doi.org/10.1109/TED.2020.2988439.

[33] M. Moll, Radiation damage in silicon particle detectors - microscopic defects and macroscopic properties. PhD Dissertation, University of Hamburg, Germany, 1999.

[34] C. B. Soh, D. Z. Chi, H. F. Lim, S. J. Chua, Comparative study of trap levels observed in undoped and Si-doped GaN, Mat. Res. Soc. Symp. Proc. 719 (2001) 135. https://doi.org/10.1557/PROC-719-F13.5.

[35] P. Kamyczek, E. P.-Popko, E. Zielony, Z. Zytkiewicz, Deep levels in GaN studied by deep level transient spectroscopy and Laplace transform deep-level spectroscopy. Mater. Sci-Pol. 31 (2013) 572-576. https://doi.org/10.2478/s13536-013-0138-0.

[36] H. Yamada, H. Chonan, T. Takahashi, T. Yamada, M. Shimizu, Deep-level traps in lightly Si-doped n-GaN on free-standing m-oriented GaN substrates, AIP Adv. 8 (2018) 045311. https://doi.org/10.1063/1.5011362.

[37] Y. Tokuda, Y. Matsuoka, H. Ueda, O. Ishiguro, N. Soejima, T. Kachi, DLTS study of n-type GaN grown by MOCVD on GaN substrates, Superlattices Microstruct. 40 (2006) 268-273. https://doi.org/10.1016/j.spmi.2006.07.025.